

# Laser ablation behavior and ablation threshold of entropy-controlled perovskite coatings

Shuo WANG<sup>1</sup>, Junyang LU<sup>1</sup>, Mengqing ZHANG<sup>1</sup>, Jiayi ZHENG<sup>1,\*</sup> and Tong ZHANG<sup>1,\*</sup>

<sup>1</sup> Chemical Defense Institute, Yangfang town, Changping district, Beijing, 102205, P.R. China

\*Corresponding author e-mail: tong zhang@126.com; zjygz 501@163.com

#### Received date:

30 June 2025

Revised date:

9 July 2025

Accepted date:

17 July 2025

#### Keywords:

Laser ablation behavior; Ablation threshold; High entropy; Reflectivity; Thermal conductivity

#### Abstract

The protection threshold of laser ablation resistant materials lags behind the development of laser power density. Single-functional laser ablation resistant materials can no longer meet the practical needs. High-entropy perovskites with infinite chemical composition, tunable bandgap structure, and efficient thermal management capabilities provide new ideas for developing novel high-reflectivity and lowthermal-conductivity multifunctional laser ablation resistant materials. Herein, leveraging these unique advantages of high-entropy perovskites in optics and thermodynamics, four entropy-controlled perovskite  $coatings, \ Ba(Zn_{1/2}Ta_{1/2})O_3 \ (BZTO), \ Ba(Zn_{1/3}Ta_{1/3}Nb_{1/3})O_3 \ (BZTNO), \ Ba(Zn_{1/4}Ta_{1/4}Nb_{1/4}Ti_{1/4})O_3 \ (BZTNO), \ Ba(Zn_{1/4}Ta_{1/4}Nb_{1/4}Ti_{1/4}Nb_{1/4}Ti_{1/4})O_3 \ (BZTNO), \ Ba(Zn_{1/4}Ta_{1/4}Nb_{1/4}Ti_{1$ (BZTNTO) and Ba(Zn<sub>1/5</sub>Ta<sub>1/5</sub>Nb<sub>1/5</sub>Ti<sub>1/5</sub>Zr<sub>1/5</sub>)O<sub>3</sub> (BZTNTZO) are designed. Through time-dependent laser ablation experiments, the optical and thermal properties are comprehensively evaluated. And laser ablation behavior and ablation threshold are systematically studied. The BZTNO achieves thermal equilibrium at 1000 W·cm<sup>-2</sup> and possesses longest ablation thresholds at different energy densities, demonstrates a superior thermal management performance. The optical reflectivity and the thermal expansion coefficient matching with the steel substrate make a major contribution to the excellent laser ablation resistant performance. The ablation thresholds of other entropy-controlled samples increase with entropy. This is attributed to the fact that the increase of cation disorder can effectively reduce the thermal conductivity. The designed entropy-controlled perovskite systems offer wide application prospect in laser ablation.

### 1. Introduction

With the rapid development of laser technology, the energy densities are rapidly increasing [1-6]. This imposed a higher demand on laser ablation resistant materials. When laser interact with materials, the optical energy is rapidly converted into thermal energy, inducing a severe damage on the surface and even inside. Therefore, the development of laser ablation resistant materials shows a great potential. Dissipating incident laser energy and limiting thermal conduction are the two critical principles for protecting the substrate. Currently, the common reported laser ablation resistant materials primarily focus on the high-reflectivity [7,8], thermal insulation [9,10], and ablation [11,12] types. Ablation-type materials can dissipate laser energy through the intense burning, but the aerodynamic shape of the equipment will be changed. Thermal insulation materials have low thermal conductivity inhibiting the heat transfer to the substrate, while the heat accumulation can cause local damage. From the optical perspective, the high-reflectivity materials effectively reduce heat deposition. However, metallic materials suffer from low melting points [13], and organic membrane materials [14,15] exhibit poor thermal stability among the reported high-reflectivity materials. Therefore, all the single-functional laser ablation resistant materials have low ablation thresholds, which have limited the application in high energy laser ablation. Developing a novel material that combines high reflectivity and low thermal conductivity is of highly significant.

To overcome the technical limitations of low reflectivity and poor thermal insulation, high-entropy perovskite materials have garnered widespread attention [16-18]. High-entropy perovskite materials inherently exhibit low thermal conductivity, high melting points and thermal stability, making them highly promising for thermal insulation applications [19-21]. These thermal properties effectively block laser energy transfer to the substrate. Furthermore, their infinite compositional design space, wide tolerance factor range (t = 0.75 to 1) and four core effects of high entropy endow the high-entropy perovskite material with a rich and highly tunable optical bandgap structure [22-24]. The synergistic interactions in high-entropy perovskites of thermal and optical properties are expected to be a new candidate for laser ablation resistant materials [25,26], offering broad application prospects. They can dissipate laser energy through reflection and reduce heat accumulation by means of low thermal conductivity, thereby protecting the substrate.

Herein, four entropy-controlled BaMO<sub>3</sub> (M=Zn, Ta, Nb, Ti, Zr) perovskite coatings were prepared, and experimentally evaluated their laser ablation resistant performance at 1000 W·cm<sup>-2</sup>, 1500 W·cm<sup>-2</sup>, 2000 W·cm<sup>-2</sup> and 2500 W·cm<sup>-2</sup>. Laser ablation behavior and ablation threshold were systematically studied. Infrared thermal imaging camera and a high-speed camera were adopted to record the temperature change of the coating and the damage of the molten pool during the irradiation process. The 3D-super-depth-digital microscopy is used to reconstruct the ablated zone for analyzing the degree of damage.

The microscopic ablation morphology was also observed. In order to further explore the role of optical and thermal properties in the laser ablation process, the reflectivity of the coating at different ablation time, thermal conductivity and thermal expansion coefficient were collected. The front-back surface temperature of the coating and the phase evolution of the coatings at different power densities were deeply analyzed. This study provides a new pathway for the application of entropy-controlled perovskite materials in the field of laser ablation resistance.

## 2. Experimental

## 2.1 Coating preparation

The four entropy-controlled powders, Ba(Zn<sub>1/2</sub>Ta<sub>1/2</sub>)O<sub>3</sub> (BZTO), Ba(Zn<sub>1/3</sub>Ta<sub>1/3</sub>Nb<sub>1/3</sub>)O<sub>3</sub> (BZTNO), Ba(Zn<sub>1/4</sub>Ta<sub>1/4</sub>Nb<sub>1/4</sub>Ti<sub>1/4</sub>)O<sub>3</sub> (BZTNTO) and  $Ba(Zn_{1/5}Ta_{1/5}Nb_{1/5}Ti_{1/5}Zr_{1/5})O_3$  (BZTNTZO), were prepared by solid-state reaction method according to our previous work with some modifications (Figure S1). All chemicals were of analytical grade without further treatment. Specifically, the as-prepared powder samples were mixed with the inorganic binder (YK-8972) in a mass ratio of 1:1. Three ZrO<sub>2</sub> grinding balls were added in the mixture to mix adequately. The mixture was then homogenized at 55 Hz for 10 min to obtain a uniformly mixed slurry. This slurry was applied to a 50 mm  $\times$  50 mm  $\times$ 2 mm steel substrate using a scraping painting method. The coatings were first curing at room temperature for 12 h. And then it was transferred to the oven for 80°C for 1 h, 100°C for 1 h, 120°C for 1 h and 150°C for 1 h, respectively. After drying and curing, the coatings were collected for subsequent characterization and laser irradiation testing. The coating thickness can be normalized by fixing the mass of the slurry adhered to the substrate. A spiral micrometer was used to measure the thickness via selecting 5 point on the coatings. The measured values were deducted from the thickness of the substrate, and the average value was taken as the actual thickness of the coating. The detailed process of laser irradiation experiment was referred to the previous report [27].

### 2.2 Characterization

The crystallinity and phase purity of the samples were characterized by X-ray diffraction (XRD) on Rigaku D/MAX-2600 (Cu Kα source,  $\lambda = 1.5418 \text{ Å}$ ) using a copper target. The analysis of element content was characterized by scanning electron microscope-energy dispersive spectrometry (SEM-EDS) performed on a ZEISS Gemini SEM-300 instrument equipped with OXFORD XPLORE30. The reflectivity was measured using a Hitachi UH-4150 spectrophotometer equipped with an integrating sphere attachment. The 3D-super-depth-digital microscopy (3D-SDDM) was adopted VHX600 (Keyence) to reconstruct the 3D surface of the sample after laser ablation. And the color photography was carried out to obtain the intuitive ablation morphology. The PT870 (Guide), PL430 (Guide) cameras and high-speed camera (SSZN, SH-2101) recorded temperature and molten pool changes during the laser irradiation. And the thermocouples equipped with multi-channel temperature recorder (TCP-700X) was adopted to collect back temperature of the coatings.

### 3. Results and discussion

### 3.1 Study on laser ablation behavior

Laser ablation resistant performance evaluation of the entropycontrolled BaMO<sub>3</sub> (M=Zn, Ta, Nb, Ti, Zr) coatings is depicted in Figure 1. To investigate the changes in coating at different stages within the ablation threshold, the fresh entropy-controlled coatings are ablated at 1500 W·cm<sup>-2</sup> during fixed time intervals. An obvious difference is existed among different samples in their laser ablation threshold. The BZTNO has optimal laser ablation resistant performance with the threshold even beyond 45 s (Figure 1(g-i)). Therefore, the time interval of 15 s is selected to observe the behavior of BZTNO coating during irradiation. For the other samples, entropy increase effectively prolongs the threshold. Similarly, the time interval of the BZTNTZO (Figure 1(a-c)), BZTNTO (Figure 1(d-f)) and BZTO (Figure 1(j-k)) samples are chosen as 5 s, 3 s and 2 s, respectively. Before reaching to the withstand maximum temperature of coating, the molten pools of irradiate center are observed no significant changes. The dynamic process of molten pool is recorded by high-speed camera. In the initial of laser irradiation, numerous fine bubbles emerge in the molten pool, which is primarily induced by the volatilization of low-melting-point substances (such as water and organic solvents) remaining in the binder. At 45 s for the BZTNO, there is little point damage in the molten pool and slightly melting occurs. Comparatively, the molten pool of the BZTNTZO at 15 s is emerged severely melted. And the BZTO has the worst performance, with noticeable bubbling even at 1000 W⋅cm<sup>-2</sup> for 2 s (Figure 1(j-k)). Such a poorest laser ablation resistant performance for BZTO can be attributed to its abundant oxygen vacancies induced by the severe charge mismatch in M-site.

To further observe the surface changes of coating during the ablation process, we employ photographs, 3D-SDDM images, and infrared thermal images of ablated coatings to analyze the damage situation at fixed time intervals, as shown in Figure 2(a-k). The schematic diagram of the irradiation process for all samples is presented in Figure 2(1). All coatings have analogous damage morphology with square-shaped ablated zone and the surrounding transition zone. The square-shaped ablated zone is covered by square-shaped light spot, forming a regular square of 1 cm × 1 cm. The laser energy diffuses from the ablated zone to the surroundings forming a transition zone. These two regions can be clearly distinguished in the infrared thermal images (Figure 2).

For the high-entropy BZTNTZO, a distinct convex-shaped ablated zone is observed in the photograph of ablated coating after 5 s (Figure 2(a)). The front surface is below to 280°C with the maximum height difference of 726.82  $\mu$ m in ablated zone. The coating still remains functional at 10 s accompanied the highest temperature slightly increasing to 380°C (Figure 2(b)), but bubbling appears near the ablated zone as heat diffusing. And the damage height difference further increases to 1289.54  $\mu$ m. During the continues irradiation, thermal strain induced microcracks propagates and further expands the ablated area which induces the area positively correlate with irradiation time. Once the heat dissipation cannot promptly offset the energy input, prolonged heat accumulation within coating raises the temperature field. According to the experimental results, the temperature at 15 s rapidly rises to 926°C, together with intensified melting in coating surface (Figure 2(c)). The

thermal damage poses a threat to the substrate. The melting for the BZTNTZO coating is mainly attributed to the formation of black Ti<sup>3+</sup>, which increases the energy absorption accompanied with creating oxygen deficiency. Consequently, the coating is rapidly destroyed (Figure 2(c)).

Similar to the BZTNTZO, the BZTNTO contains a higher concentration of Ti, exhibits a degenerative laser ablation resistant performance (Figure 2(d-f)). The ablation center of coating surface undergoes severe melting at 9 s, forming a black and glass-like ablation spot. The maximum height difference in the ablated zone reaches  $3153.12 \ \mu m$ .

Free from the interference of Ti element, the BZTNO exhibits a significant improvement in laser ablation resistant performance. As the infrared thermal images depicted in Figure 2(g-i), the maximum

temperature of the ablated zone is  $339^{\circ}$ C,  $375^{\circ}$ C and  $388^{\circ}$ C with the irradiation time increased from 15 s to 45 s. The slight temperature rise reflects the robust laser ablation resistance performance. The surface morphology from the photograph at 45 s shows that there is only slight melting occurs at the ablated surface, allowing the coating to remain functional (Figure 2(g-i)). Compared to the mark at 15 s, their maximum height difference of the damage increases about  $2000 \ \mu m$ .

The BZTO develops a white bubble on the coating surface with a height of 2499.20  $\mu m$  and the area of 1 cm  $\times$  1 cm, when irradiated at 1000 W·cm<sup>-2</sup> for 2 s (Figure 2(j-k)). And there is a rapid temperature rise from 240°C to 430°C in ablated zone after irradiation of 4s, as the infrared thermal images reveals. Meanwhile, the ablated area expands and the bubble height increases to 3552.8  $\mu m$ .

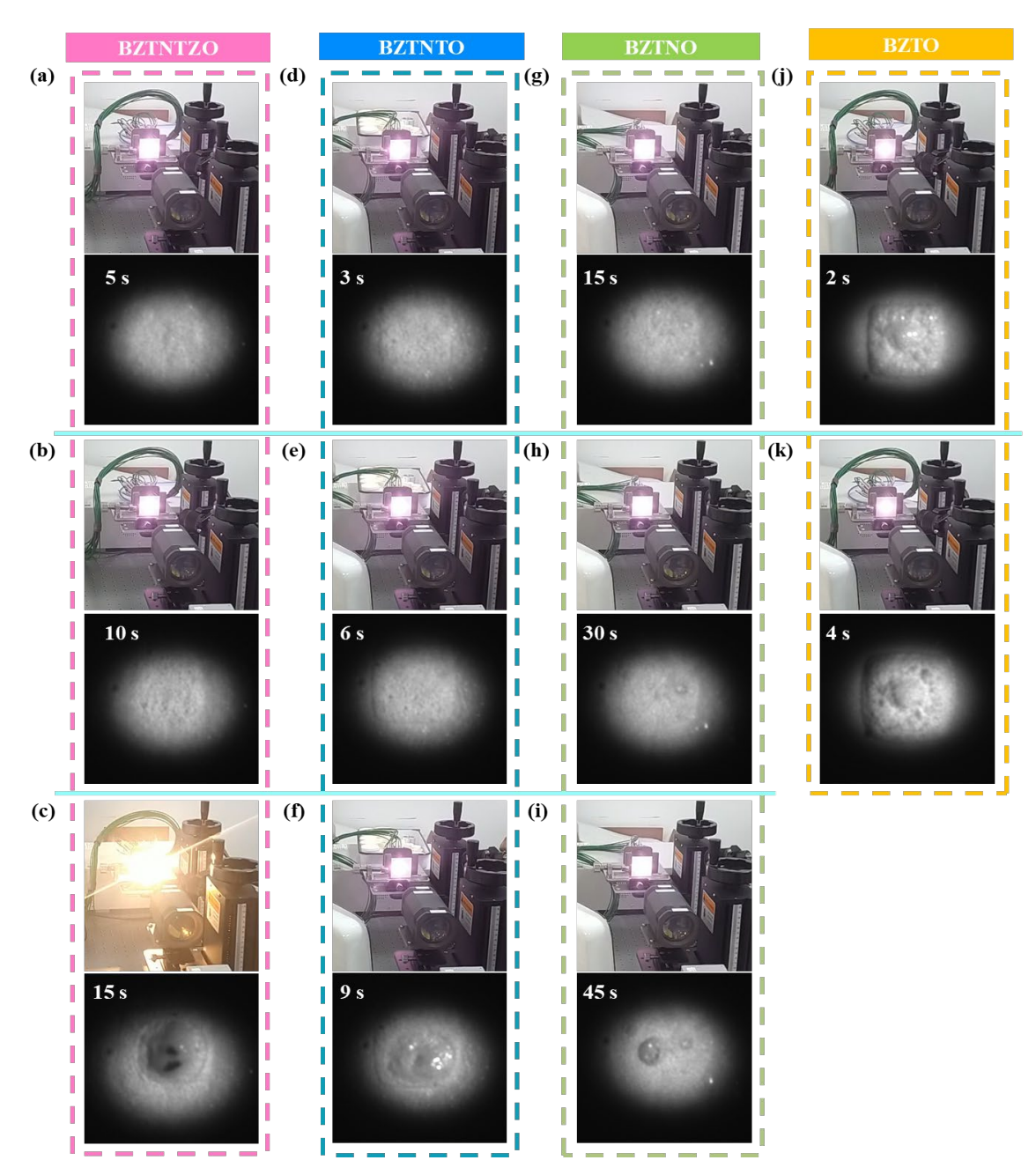


Figure 1. Irradiation status (top) and in-situ molten pools (below) of (a-c) BZTNTZO, (d-f) BZTNTO, and (g-i) BZTNO at 1500 W·cm<sup>-2</sup>, and (j-k) BZTO at 1000 W·cm<sup>-2</sup> during fixed time intervals.

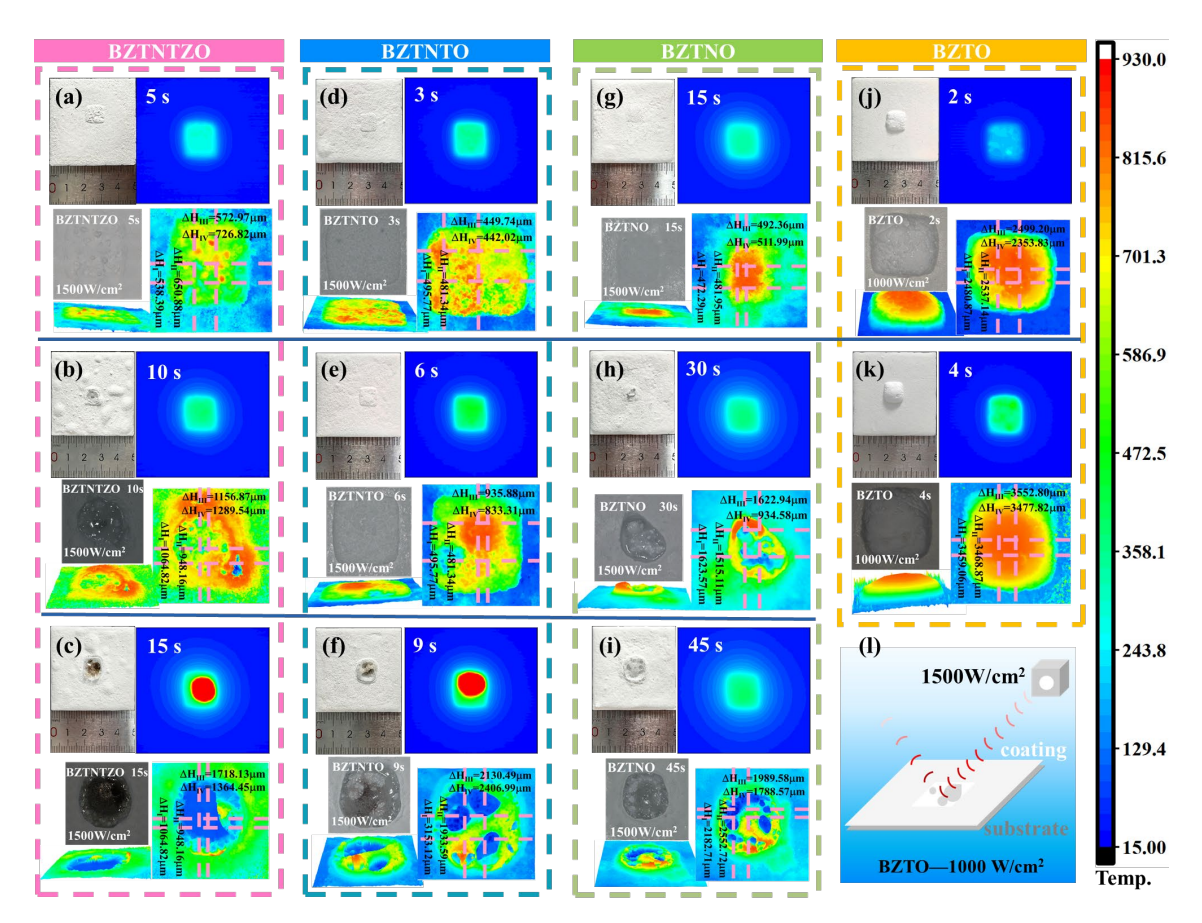


Figure 2. The damage conditions of the entropy-controlled samples after different ablation times at an energy density of  $1500 \text{ W} \cdot \text{cm}^{-2}$ . Photograph of coating (top left), infrared thermal images (top right), and 3D-SDDM (bottom) of BZTNTZO (a-c), BZTNTO (d-f), BZTNO (g-i), BZTO (j-k) (using  $1000 \text{ W} \cdot \text{cm}^{-2}$ ), and (i) Schematic diagram of the irradiation process.

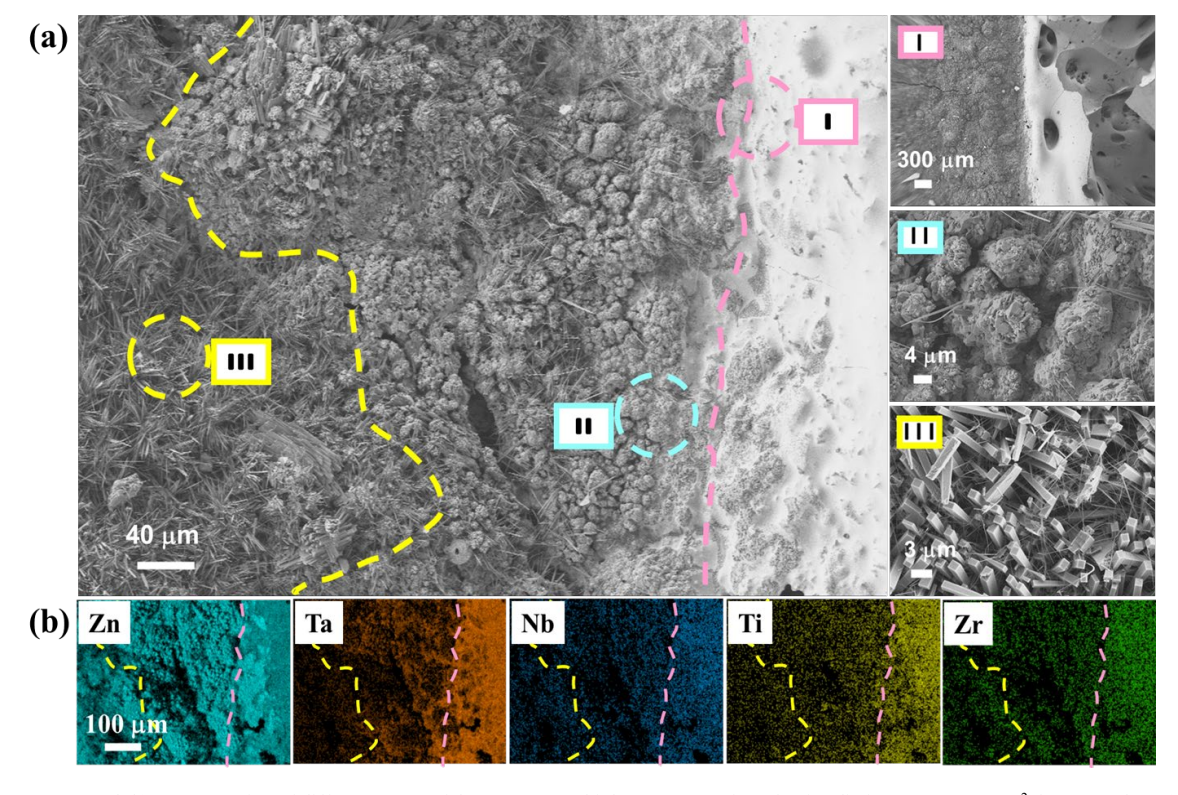


Figure 3. (a) SEM and (b) EDS mapping of different zones of the BZTNTZO high-entropy coating after irradiation at 1500 W·cm<sup>-2</sup> for 15 s, where (I) ablated zone, (II) transition zone, and (III) unablated zone.

The microstructure of the high-entropy BZTNTZO coating is further observed by SEM, as Figure 3 displays. Fresh prepared entropycontrolled coatings are shown in Figure S2. The perovskite particles in the coatings are uniformly distributed with rod-shaped and needlelike particles from the binder, indicating a well-mixed slurry (Figure 3). And the surface exhibits no obvious cracks or bubbles. Furthermore, the ablated coatings exhibit three distinct parts with clear boundaries: ablated zones (I), transition zones (II), and unablated zones (III). In the transition zone (Zone II), it is evident that the high-entropy perovskite particles are encapsulate to form spherical clusters by the softeningdeformation binder at high temperature. The surface of ablated zone (Zone I) is primarily composed of a smooth, glassy structure formed by the rapid cooling and solidification of the melted binder (Figure 3). Perovskite particles are observed embedded within the recrystallized glassy structure upon the magnification of ablated zone. This indicates that the perovskite particles have not reached their melting point before irradiation ceased, and the coating has not completely failed (Figure S3). Additionally, the glassy structure exhibits numerous large pores and sharp fractures. The large pores are produced by the rapid vaporization of low-melting-point substances in the binder at high temperatures, breaking through the molten surface. And the sharp fractures are result from rapid contraction during the cooling. From the EDS mapping in Figure 3, it can be observed that the incorporated transition metal elements are uniformly distributed across the three zones. Furthermore, the STEM mapping in Figure S4 reveals that the transition metal elements within the perovskite particles remain uniformly distributed in the ablated zone.

To further investigate the laser ablation behavior of the entropycontrolled coatings, their reflectivity is studied. As shown in Figure 4(a), all samples exhibit high reflectivity before laser irradiation. Except for the BZTNO sample, the reflectivity of the coatings generally increases with entropy. The high-entropy sample BZTNTZO has a reflectivity of 95.9% at 1064 nm, higher than that of the medium-entropy sample BZTNTO (94.7%) and the low-entropy sample BZTO (85.5%). Changes in entropy are influenced by the radius and valence state of newly introduced ions, having a significant effect on the band structure [28].

Particularly, the BZTNO exhibits the highest reflectivity of 98.1% among them, even surpassing that of the high-entropy BZTNTZO. The high reflectivity can dissipate laser energy through reflection during laser irradiation, reducing energy deposition and achieving the purpose of protecting the substrate. Therefore, the reflectivity of the BZTNO is one of critical factor contributing to its optimal laser ablation resistant performance from an optical perspective. Another important factor is the thermal properties. Regarding the coefficient of thermal expansion (CTE), the BZTNO sample  $(12.161 \times 10^{-6} \, ^{\circ}\text{C}^{-1})$ has a closer match to the steel substrate  $(11.0 \times 10^{-6.\circ} \text{C}^{-1} \text{ to } 12.5 \times 10^{-6.\circ} \text{C}^{-1})$ 10<sup>-6.</sup>°C<sup>-1</sup>) (Table 1). This characteristic allows the BZTNO coating to minimize thermal strain during laser irradiation, improve thermal shock resistance, and quickly adapt to temperature changes. Its CTE also enhances interfacial bonding strength, preventing coating cracking or peeling, thereby effectively reducing thermal fatigue and failure risks. Furthermore, although the thermal conductivity shows a decreasing trend with entropy in Table 1, all samples exhibit significantly lower thermal conductivity compared to the steel substrate. This demonstrates all the entropy-controlled samples can generally achieve an effective thermal insulation performance.

During laser irradiation, the reflectivity decreases with prolonged irradiation time (Figure 4(b-e)). For the BZTNO, the reflectivity at 1064 nm is 97.9%, 72.9%, and 62.7% after irradiation for 25 s, 45 s and 65 s, respectively (Figure 4(d)). The generation of oxygen vacancies during laser ablation process induces this reflectivity attenuation, since the formation energy of oxygen vacancies is much lower than other elements. The instantaneous laser ablation easily causes oxygen atoms to escape from the lattice, forming oxygen vacancies. These vacancies act as absorption centers, leading to a decrease in reflectivity over time.

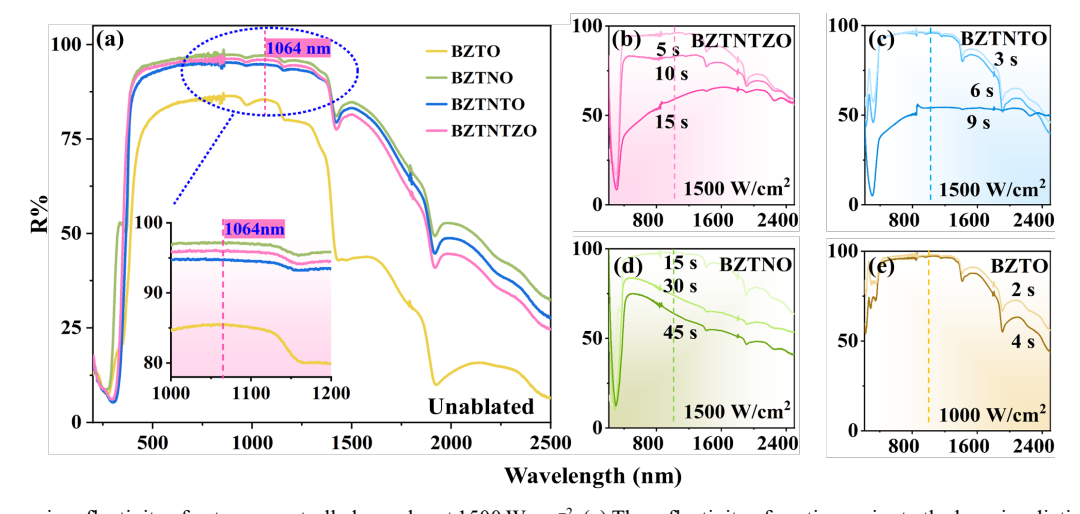


Figure 4. Changes in reflectivity of entropy-controlled samples at  $1500~\rm W\cdot cm^{-2}$ . (a) The reflectivity of coatings prior to the laser irradiation experiment. The reflectance of (b) BZTNTZO, (c) BZTNTO, (d) BZTNO and (e) BZTO (in  $1000~\rm W\cdot cm^{-2}$ ) at different ablation times.

Table 1. Thermal conductivity and thermal expansion coefficient.

	BZTO	BZTNO	BZTNTO	BZTNTZO	1045 Steel
Thermal conductivity W·m <sup>-1</sup> ·K <sup>-1</sup>	2.827 (8)	2.077 (2)	1.299 (8)	1.141 (2)	45-55
$CTE \times 10^{-6} \cdot {}^{\circ}C^{-1}$	13.039	12.161	13.369	7.220	11.0~12.5

Furthermore, as shown in Figure 4(b-c), the reflectivity of the BZTNTZO and BZTNTO samples decreases more significantly than that of other samples. This can be attributed that some Ti<sup>4+</sup> convert to Ti<sup>3+</sup>, introducing impurity levels near the conduction band. These impurity levels increase the photons absorption (Figure 4(b-c)). Moreover, the black Ti<sup>3+</sup> as a color center further accelerates absorption. These are the primary reasons for the rapid decline in reflectivity and accelerating coating failure in the BZTNTZO and BZTNTO samples during laser ablation. Meanwhile, it is also another key factor contributing to the weaker laser ablation resistant performance of high-entropy samples compared to BZTNO.

Interestingly, the reflectivity of the BZTO increases during irradiation (Figure 4(e)). The BZTO contains the valence mismatch ions of Zn<sup>2+</sup> and Ta<sup>5+</sup>, generating a large number of oxygen vacancies. During the early stages of laser irradiation, the BZTO sample experiences an oxygen replenishment process, increasing in reflectivity [29].

Figure 5 compares the peak temperature differences between the front and back surfaces of the coatings at these three irradiation times. The BZTNO shows the smallest front-to-back temperature difference (327.77°C) after 45 s, with a front surface temperature of only 416.5°C. This indicates that the coating remains in good condition, with no significant degradation in laser ablation resistant performance. This result is attributed to the synergistic effects of high reflectivity and low thermal conductivity in the BZTNO, rapidly dissipating the laser energy to protect the substrate. However, the temperature difference of the high-entropy BZTNTZO is 379.70°C at first 5 s. And the coating remains stable during this period. At 10 s, the difference significantly increases to 1189.32°C, causing the coating to begin melting (Figure 1(b) and Figure 2(b)). It indicates that the incident energy on the front surface substantially exceeds the dissipated energy. The created melting point can quickly break down the coating. The temperature difference rapidly increases at 15 s, corresponding to the onset of ablation damage and coating failure (Figure 1(c) and Figure 2(c)). The behavior of the BZTNTO is similar to that of the high-entropy BZTNTZO. In contrast, the BZTO exhibits the poorest laser ablation resistant performance. Even when tests at 1000 W·cm<sup>-2</sup>, the temperature difference doubled from 2 s to 4 s, leading to rapid coating failure (Figure 1(j-k) and Figure 2(j-k)). Furthermore, the remarkable temperature differentials on the front surface between the entropy-controlled coatings is primarily attributed to reflectivity and thermal diffusion. The reflectivity can minimize the absorption of laser energy. When reflectivity values are comparable, thermal diffusion becomes the predominant governing factor for front surface temperature. A well-matched CTE with the substrate facilitates rapid energy dissipation from the ablation center, thereby reducing thermal accumulation. The BZTNO sample demonstrates both the highest reflectivity and optimal CTE matching with the substrate. This unique combination enables highly efficient thermal management.

#### 3.2 Study on laser ablation threshold

Based on the above research on the laser ablation behavior, we study the laser ablation threshold of the four entropy-controlled samples. Laser ablation tests are conducted at energy densities of 1000 W·cm<sup>-2</sup>, 1500 W·cm<sup>-2</sup>, 2000 W/cm<sup>2</sup>, and 2500 W·cm<sup>-2</sup>. The ablation threshold of coatings here is defined as the moment when sparks first appear. The experimental results are summarized in Table 2. The BZTNO exhibits the best laser ablation resistant performance across all energy densities. This result is consistent with the analysis of the ablation behavior. Except for the BZTNO, the high-entropy BZTNTZO has longer ablation threshold among the other samples, especially in 1000 W⋅cm<sup>-2</sup>. The BZTNTZO and BZTNO withstood continuous ablation for over 300 s at 1000 W⋅cm<sup>-2</sup> without failure. The ablation threshold of at different energy densities increases with entropy. The ablation threshold of high-entropy BZTNTZO is 5 time longer than that of BZTO sample and 1.45 time of BZTNTO sample at 1500 W·cm<sup>-2</sup>. At 2000 W·cm<sup>-2</sup>, the ablation threshold of the BZTNTZO is twice of the BZTNTO.

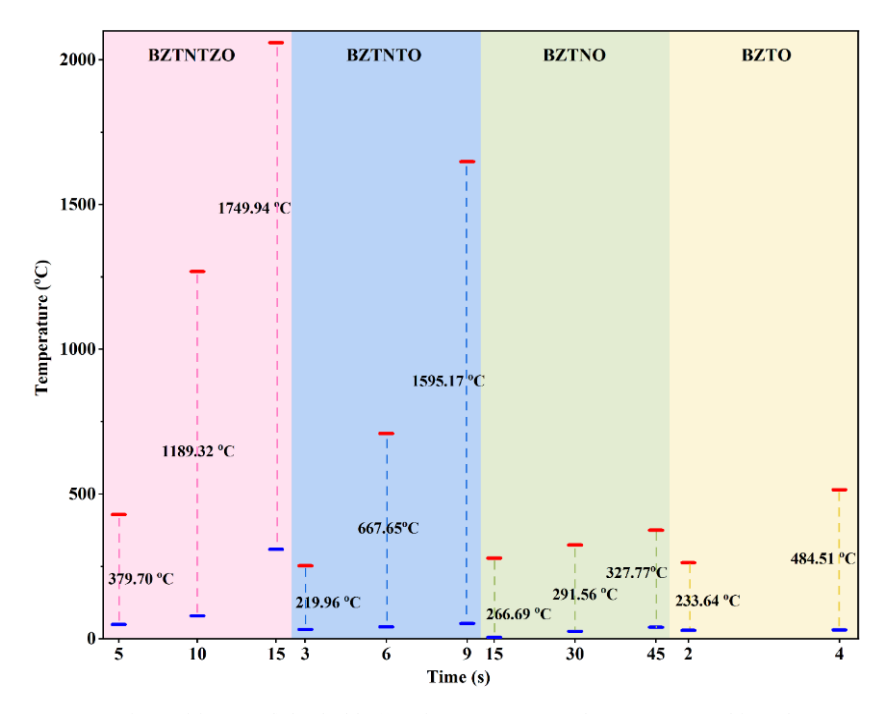


Figure 5. The peak temperature comparison of front (red)-back (blue) surface temperature (the BZTO was subjected at 1000 W·cm<sup>-2</sup>).

Table 2. Ablation threshold of entropy-controlled samples under different energy densities.

	1000 W⋅cm <sup>-2</sup>	1500 W⋅cm <sup>-2</sup>	2000 W·cm <sup>-2</sup>	2500 W·cm <sup>-2</sup>	
	[s]	[s]	[s]	[s]	
BZTO	8	3			
BZTNO	300	51	18	4	
BZTNTO	51	11	5.5	3	
BZTNTZO	300	16	11.5	3	

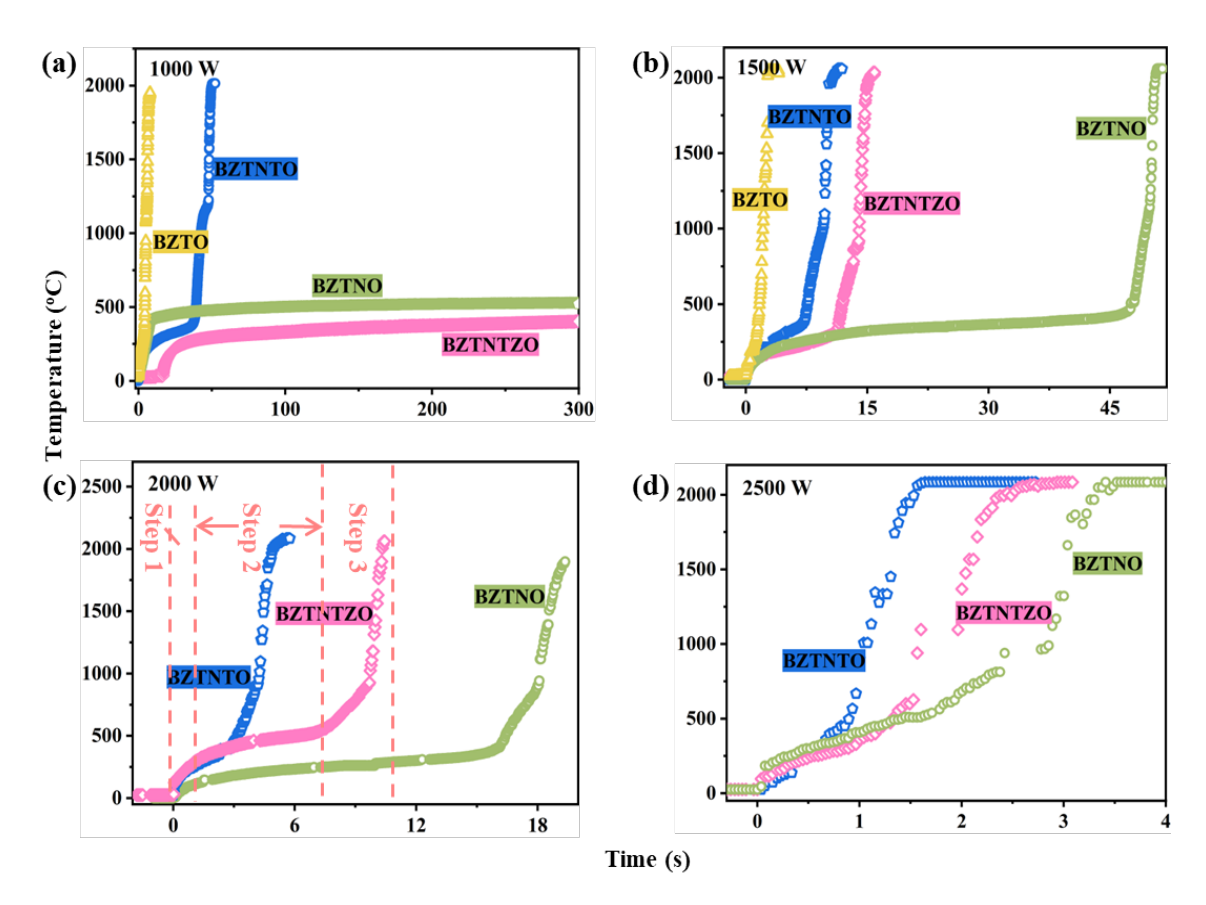


Figure 6. The front surface temperature curves of the entropy-controlled samples at (a) 1000 W·cm<sup>-2</sup>, (b) 1500 W·cm<sup>-2</sup>, (c) 2000 W·cm<sup>-2</sup>, and (d) 2500 W·cm<sup>-2</sup> energy densities.

Figure 6 compares the changes in the front surface temperature of coatings after reaching their ablation threshold. Similarly, all samples experience a three-step heating process under different energy densities. Taking the high-entropy BZTNTZO at 2000 W·cm<sup>-2</sup> in Figure 6(c) as an example, the steps are as follows: rapid heating from 0 s to 1 s (Step 1), slow heating or reaching thermal equilibrium from 1 s to 8 s (Step 2), and rapid heating again from 8 s to 11 s (Step 3).

During the initial stage of laser irradiation (Step 1), the high energy density of the laser is directly imparted onto the coating surface. Laser energy is mostly instantaneously converted into thermal energy. The heat cannot dissipate rapidly owing to their inherent time lag associated with thermal diffusion and conduction processes, driving a sharp increase in surface temperature. This stage is short in duration, with minimal variation observed among these samples, and is typically completed within 1 s.

The slow heating or thermal equilibrium stage (Step 2) serves as a comprehensive evaluation of the photothermal properties of the coating. During this stage, the front surface temperature of the entropy-

controlled samples generally contrary to the trend of entropy increase. At 1000 W·cm<sup>-2</sup> in Figure 6(a), the high-entropy BZTNTZO and BZTNO in Step 2 achieve thermal equilibrium, characterized by a nearly constant temperature. The thermal equilibrium indicates that the internal and surface temperatures of the coating gradually converge during this period, and the heat absorbed by the coating balances the energy dissipated through radiation, convection, and conduction. They maintain stable even more than 300 s, which is approximately 8 time longer than that of the BZTNTO sample and 50 time of the BZTO. At the energy densities of 1500 W·cm<sup>-2</sup> and 2000 W·cm<sup>-2</sup>, the entropycontrolled samples demonstrate a similar trend in stabilization time during Step 2 (Figure 6(b-c)). This is attributed to the fact that entropy increase can effectively reduce the thermal conductivity (Table 1) [30-33]. Constrained by the thermal conductivity and thermal diffusion, the rate of temperature rise slows down. For the BZTO, as discussed above, the valence mismatch induces a lower reflectivity (Figure 4), and the low entropy gives it a higher thermal conductivity (Table 1). Therefore, the BZTO shows poorest laser ablation resistant performance.

During 2500 W·cm<sup>-2</sup>, all coatings experience a rapid temperature rise and failure within a short period. A minimal difference is existed among four coatings.

With continuous irradiation, the aluminosilicate in the binder begins to melt and even develop damage points. The melting and damage of the coating promote laser absorption, further accelerating the heating process. Therefore, Step 3 is reentering a rapid heating, characterized by a short duration and rapid temperature rise. Most coatings in this step reach their ablation threshold and the temperatures even exceed the measurement range. Additionally, a feedback effect is observed in the BZTNTO and BZTNTZO samples. The generation of Ti<sup>3+</sup> among them is darken the coating surface and sharply dropped the reflectivity, significantly enhancing absorption (Figure 2(c,f)).

Figure 7(a-d) compares the changes of the back surface temperature at their ablation thresholds. The trends of back temperatures are consistent with their front surface temperatures. Limited by thermal retardation effects, the back surface temperature rise is relatively delayed. It primarily experiences two steps: slow heating and rapid heating [34,35], corresponding to the changes in front surface temperature. Since the BZTNTZO and BZTNO both achieve thermal equilibrium at  $1000~\rm W\cdot cm^{-2}$ , the back surface temperature rises slowly in the long equilibrium (Figure 7(a)). However, compared with Figure 6(a), although the front surface temperature of the BZTNO is higher than that of the high-entropy BZTNTZO, the back surface temperature of the BZTNO is lower. Additionally, from the perspective of long-term heat accumulation (Figure 6(a)), the temperature difference at

the thermal equilibrium stage in the BZTNO sample (99°C) is lower than that in the BZTNTZO (196°C). And the BZTNO displays no significant ablation marks on the coating surface even after 300 s of irradiation, as observed in Figure S5. Therefore, the BZTNO exhibits superior laser ablation resistant performance. Except for the BZTNO with exceptional performance, samples with higher entropy values show lower back temperatures. This is a result of entropy engineering, which enables efficient thermal management (Table 2). Heat must transfer from the front surface of the coating to the back via thermal conduction, so high-entropy samples with lower thermal conductivity typically exhibit lower back surface temperatures compared to mediumand low-entropy samples. However, for BZTNTO and BZTO samples, even though the front-surface temperature of the coating exceeds 2000°C, the back temperature remains below 100°C. It has not been completely penetrated, still possessing the function of protecting the substrate. Because the laser only damages the superficial layer of the coating (Figure 2(f,k)).

This large front-to-back surface temperature difference is also observed at the energy densities of 1500 W·cm<sup>-2</sup>, 2000 W·cm<sup>-2</sup>, and 2500 W·cm<sup>-2</sup> (Figure 7b-d). Furthermore, we also observed that the maximum back temperature decreases as the laser energy density increases. This is because the rapid ablation process at high energy densities has a shorter duration, leaving insufficient time for conducting the energy to the back. Furthermore, the phase transition of the coating during the short ablation period also consumes a portion of the energy.

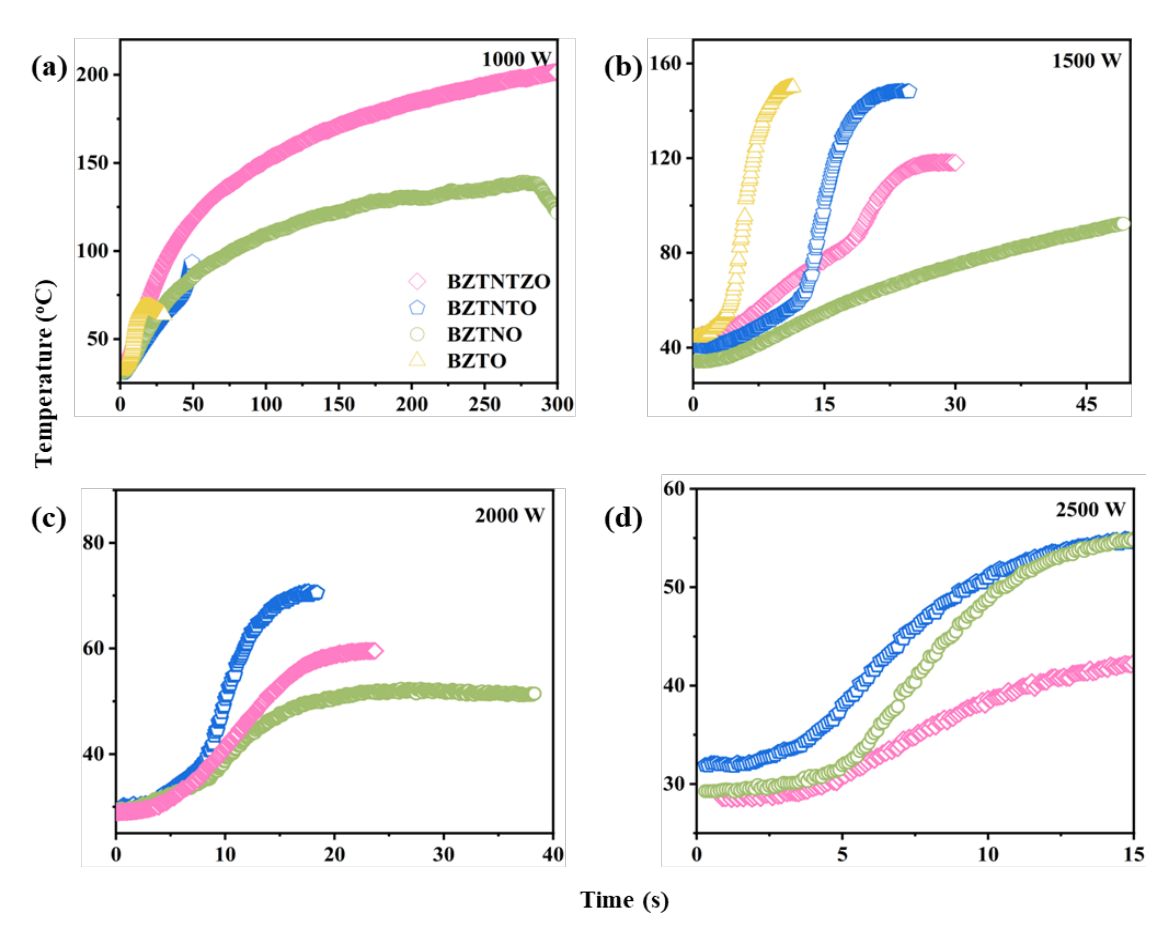


Figure 7. The back surface temperature curves of the entropy-controlled samples at energy densities of (a) 1000 W·cm<sup>-2</sup>, (b) 1500 W·cm<sup>-2</sup>, (c) 2000 W·cm<sup>-2</sup>, and (d) 2500 W·cm<sup>-2</sup>.

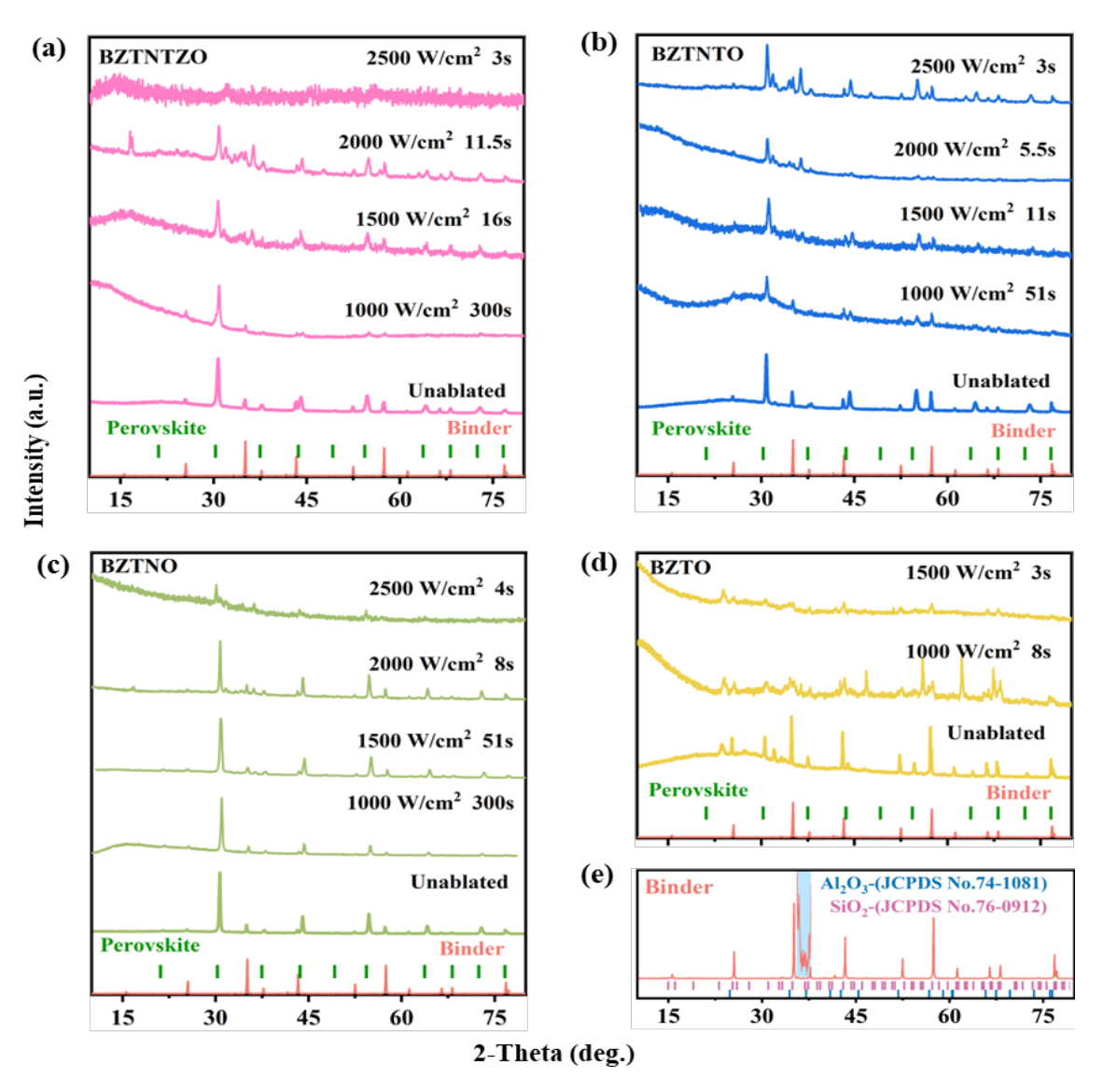


Figure 8. XRD patterns of (a) BZTNTZO, (b) BZTNTO, (c) BZTNO, (d) BZTO, and (e) the binder.

The phase evolution process of the coatings under different power densities has been further studied, as Figure 8 manifested. The phase composition of the four unablated samples consists of a mixture phase of perovskite (JCPDS No. 82-1891) and binders (Al<sub>2</sub>O<sub>3</sub>-(JCPDS No.74-1081) and SiO<sub>2</sub>-(JCPDS No.76-0912)). However, there are many fresh peaks generated after laser ablation in Figure 8(a-d). And with the laser energy density increases, these peaks increase. The relative peak intensities have significantly changed, presenting amorphous phase gradually. Surprisingly, these peaks maintain well correspondence with the standard cards of Al<sub>2</sub>O<sub>3</sub> ( JCPDS No.74-1081) and SiO<sub>2</sub> (JCPDS No.76-0912), as figure 8(e) demonstrated. Therefore, these peaks are not impurity peaks. As observed in Figure 3, these are original from the orientation and deformation of particles in the binder under high temperatures. It means that the failure of the coating mainly comes from the destruction of the binder at high temperature. But for the BZTNTZO and BZTNO coatings at 1000 W⋅cm<sup>-2</sup> in Figure 8 (a,c), the phase structures have no significant changes even after 300 s of irradiation. This further indicates that perovskite oxides with excellent thermal management properties can minimize binder melting, thus effectively protecting the coating.

### 4. Conclusions

In this work, we successfully prepared four entropy-controlled perovskite coatings on the steel substrate. The coatings were experienced laser ablation at four different energy densities of 1000 W·cm<sup>-2</sup>, 1500 W·cm<sup>-2</sup>, 2000 W·cm<sup>-2</sup>, and 2500 W·cm<sup>-2</sup>, to investigate laser ablation behavior and the ablation threshold. A comprehensive analysis was conducted on the ablation morphology, damage situation, front/back surface temperature, phase composition, optical properties, and thermal properties of the ablated coatings. The study found that the BZTNO sample displayed optimal reflectivity and a thermal expansion coefficient that matched the substrate. These characteristics improved the interfacial bonding strength between the coating and the substrate, minimized thermal strain and heat deposition during laser irradiation. These advantages enabled the coating to quickly adapt to rapid temperature changes. As a result, the BZTNO exhibited superior ablation resistant performance across various energy densities. Additionally, the highentropy BZTNTZO exhibited exceptional thermal management performance at 1000 W·cm<sup>-2</sup>, making it more suitable for low-energydensity and long-duration protection. This research confirmed that

high reflectivity, low thermal conductivity, and a substrate-matched thermal expansion coefficient were critical for achieving laser ablation resistant and provided valuable guidance for the development of multifunctional laser ablation resistant materials.

### Acknowledgements

This work was financially supported by National Natural Science Foundation of China (Grant Number 52402097) and China Postdoctoral Science Foundation (Grant Number GZC20233569).

### References

- [1] C. Wan, P Xia, J. Hua, X. Chen, W. Lang, W. Xue, Y. Geng and T. Fang, "Fabrication of SiC composites by selective laser sintering and reactive melt infiltration," *Ceramics International*, vol. 51, no. 11, pp. 14842-14851, 2025.
- [2] Z. Yong, Y. Wang, G. Yang, Y. Shi, Q. Zhang and J. Yao, "Optimization for furnace-assisted laser cladding process parameter of crack-free ceramic-based coating by response surface methodology," *Ceramics International*, vol. 51, no. 9, pp. 11735-11746, 2025.
- [3] Y. Wang, Q. Peng, G. Wu, J. Yao, Y. Yin, L. Li, Y. Zheng and C. Wen, "Effect of auxiliary laser irradiation on characteristics and properties of micro-arc oxidation coating on Ti<sub>6</sub>Al<sub>4</sub>V alloy," *Ceramics International*, vol. 50, pp. 19412-19423, 2024.
- [4] M. Fabey, "USN demonstrates high-energy laser weapon system," Jane s defence weekly: IHS Jane s defence weekly, vol.1, pp. 59, 2022.
- [5] H. Kaushal, and G. Kaddoum, "Applications of lasers for tactical military operations," *IEEE Access*, vol. 5, pp. 20736-20753, 2017.
- [6] J. Cook, "High-energy laser weapons since the early 1960s," Optical Engineering, vol. 52, p. 021007, 2013.
- [7] M. Li, L. Gao, Z. Ma, and X. Tian, "Study of highly reflective ceramic glaze coating and laser irradiation effects," *Materials & Design*, vol. 233, p. 112279, 2023.
- [8] J. Zheng, Z. Li, M. Zhang, L. Gao and T. Zhang, "New type of coatings combining invisibility and high power laser protection function," *Ceramics International*, vol. 50 pp. 11442-11450, 2024.
- [9] Q. Li, N. Zhang, Y. Gao, Y. Qing, Y. Zhu, K. Yang, J. Zhu, H. Wang, Z. Ma, L. Gao, Y. Liu, and J. He, "Effect of the coreshell structure powders on the microstructure and thermal conduction property of YSZ/Cu composite coatings," *Surface* & Coatings Technology, vol. 424, p.127658, 2021.
- [10] H. Ma, H. Liu, J. Shen, J. Luo, and X. Zhou, "Optical and thermal insulation properties of silica aerogel under a 7 kW·cm<sup>-2</sup> power laser irradiation," *Ceramics International*, vol. 48, pp. 16584-16598, 2022.
- [11] C. Ma, Z. Ma, L. Gao, Y. Liu, T. Wu, F. Wang, and H. Ishida, "Ablation behavior of boron-modified phenolic resin irradiated by highenergy continuous-wave laser and its evolution of carbon structure," *Materials & Design*, vol. 180, p. 107954, 2019.
- [12] F. Xu, S. Zhu, Z. Ma, H. Liu, Y. Chen, and T. Wu, "Effect of TaSi<sub>2</sub>/ZrSi<sub>2</sub> on ablation properties of carbon-phenolic composite

- irradiated by high-intensity continuous laser," *Ceramics International*, vol.46, pp. 28443-28450, 2020.
- [13] X.-T. Luo, S.-P. Li, G.-C. Li, Y.-C. Xie, H. Zhang, R.-Z. Huang, and C.-J. Li, "Cold spray (CS) deposition of a durable silver coating with high infrared reflectivity for radiation energy saving in the polysilicon CVD reactor," *Surface & Coatings Technology*, vol. 409, p. 126841, 2021.
- [14] S. Son, Y. Liu, D. Chae, and H. Lee, "Cross-linked porous polymeric coating without a metal-reflective layer for sub-ambient radiative cooling," ACS Applied Materials & Interfaces, vol. 12, no. 52, pp. 57832-57839, 2020.
- [15] Y. Zhang, X. Tan, G. Qi, X. Yang, D. Hu, P. Fyffe, and X. Chen, "Effective radiative cooling with ZrO<sub>2</sub>/PDMS reflective coating," *Solar ,Energy Materials and Solar Cells*, vol. 229, p. 111129, 2021.
- [16] S. Panda, S. Barik, R. Sahu, A. Sahu, S. Mishra, and S. K. Parida, "Studies of structural, microstructural, dielectric, and electrical characterization of BiNaZnMoO<sub>6</sub> double perovskite," *Journal* of Metals, Materials and Minerals, vol. 35, no. 2, pp. e2244, 2025.
- [17] S. Nie, L. Wu, Q. Zhang, Y. Huang, Q. Liu, and X. Wang, "High-entropy-perovskite subnanowires for photoelectrocatalytic coupling of methane to acetic acid," *Nature Communications*, vol. 15, p. 6669, 2024.
- [18] L. Su, H. Huyan, A. Sarkar, W. Gao, X. Yan, C. Addiego, R. Kruk, H. Hahn, and X. Pan, "Direct observation of elemental fluctuation and oxygen octahedral distortion-dependent charge distribution in high entropy oxides," *Nature Communications*, vol.13, pp. 2358, 2022.
- [19] P. Zhang, Z. Lou, L. Gong, J. Xu, Q. Chen, M. J. Reece, H. Yan, Z. Dashevsky and F. Gao, "High-entropy MTiO<sub>3</sub> perovskite oxides with glass-like thermal conductivity for thermoelectric applications," *Journal of Alloys and Compounds*, vol. 937, p.168366, 2023.
- [20] S. Chaowakarnkool, K. Uttarasak, S. Jaipayuk, N. Jantaping, and M. Tuiprae, "The effect of Fe-NiMnMo high entropy alloy electrode on enhancing the weldability and mechanical properties of railway steel 900A," *Journal of Metals, Materials and Minerals*, vol. 35, no. 1, pp. e2292, 2025.
- [21] Z. Zhang, L. Chu, J. Zhao, B. Xu, and Q. Ye, "Phase separation promotes FCC-phase mechanical twinning in AlCoCrFeMo<sub>0.05</sub>Ni<sub>2</sub> high entropy alloy," *Journal of Metals, Materials and Minerals*, vol. 34(3), pp. 2107, 2024.
- [22] X. Li, Z. Qiang, G. Han, S. Guan, Y. Zhao, S. Lou, and Y. Zhu, "Enhanced redox electrocatalysis in high-entropy perovskite fluorides by tailoring d-p hybridization," *Nano-Micro Letters*, vol.16, p. 55, 2024.
- [23] M. Mahboub, O. Ali, S. Zeroual, G. Rihia, M. Mimouni, I. Hamadneh, S. Bayou, H. Boulahbel, A. Benarfa, and F. Rehouma, "Influence of Bi substitution on structural and optical properties of LaFeO<sub>3</sub> perovskite," *Journal of Metals, Materials and Minerals*, vol. 34, no. 4, p. 1837, 2024.
- [24] Z. J. Corey, P. Lu, G. Zhang, Y. Sharma, B. X. Rutherford, S. Dhole, P. Roy, Z. Wang, Y. Wu, H. Wang, A. Chen, and Q. Jia, "Structural and optical properties of high entropy (La, Lu, Y, Gd,

- Ce)AlO<sub>3</sub> perovskite thin films," *Advanced Science*, vol. 9, p. 2202671, 2022.
- [25] F. Jia, S. Xu, S. Hu, J. Chen, Y. Wang, Y. Li, W. Ren, and J. Cheng, "Understanding the intrinsic piezoelectric anisotropy of tetragonal ABO<sub>3</sub> perovskites through a high-throughput study," npj Computational Materials, vol. 11, p. 6, 2025.
- [26] Y. Wang, X. Li, J. Luo, B. F. Woodfield, X. Wang, T. Feng, N. Yin, Q. Shi, G. Li, and L. Li, "An unexpected decrease in vibrational entropy of multicomponent rutile oxides," *Journal of the American Chemical Society*, vol.146, pp. 14493-14504, 2024.
- [27] Z. Li, S. Wang, M. Zhang, J. Zheng and T. Zhang, "New type of high-power laser protection coatings with both high reflectivity and low thermal conductivity," *Ceramics International*, vol. 51, pp. 3176-3184, 2025.
- [28] H. Zou, Y. Qi, S. Du, Y. Bao, X. Xin, W. Fan, Y. Xiao, S. Jin, Z. Feng, and F. Zhang, "Insight into the rate-determining step in photocatalytic Z-scheme overall water splitting by employing a series of perovskite RTaON<sub>2</sub> (R = Pr, Nd, Sm, and Gd) as model photocatalysts," *Journal of the American Chemical Society*, vol. 146, no. 41, pp. 28182-28189, 2024.
- [29] J. Zhu, Z. Ma, Y. Gao, L. Gao, V. Pervak, L. Wang, C. Wei, and F. Wang, "Ablation behavior of plasma-sprayed La<sub>1-x</sub>Sr<sub>x</sub>TiO<sub>3+δ</sub> coating irradiated by high-intensity continuous laser," ACS Applied Materials & Interfaces, vol. 9, pp. 35444-35452, 2017.
- [30] H. Chen, J. Fu, S. Huang, Y. Qiu, E. Zhao, S. Li, J. Huang, P. Dai,

- H. Fan, and B. Xiao, "Realization of fine-tuning the lattice thermal conductivity and anharmonicity in layered semiconductors via entropy engineering," *Advanced. Materials*, vol. 36, p. 2400911, 2024.
- [31] X. Kong, L. Yang, F. Meng, T. Zhang, H. Zhang, Y. Lin, H. Huang, S. Zhang, J. Guo, and C. Nan, "High-entropy engineered BaTiO<sub>3</sub>-based ceramic capacitors with greatly enhanced high-temperature energy storage performance," *Nature Communications*, vol. 16, pp. 885, 2025.
- [32] Z. Wen, Z. Tang, Y. Liu, L. Zhuang, H. Yu, and Y. Chu, "Ultrastrong and high thermal insulating porous high-entropy ceramics up to 2000°C," *Advanced Materials*, vol. 36, p. 2311870, 2024.
- [33] Y. Liu, P. Tuo, F. Dai, Z. Yu, W. Lai, Q. Ding, P. Yan, J. Gao, Y. Hu, Y. Hu, Y. Fan, and W. Jiang, "A highly deficient mediumentropy perovskite ceramic for electromagnetic interference shielding under harsh environment," *Advanced Materials*, vol. 36, p. 2400059, 2024.
- [34] Q. Li, N. Zhang, Y. Gao, Y. Qing, Y. Zhu, K. Yang, J. Zhu, H. Wang, Z. Ma, L. Gao, Y. Liu, and J. He, "Effect of the core-shell structure powders on the microstructure and thermal conduction property of YSZ/Cu composite coatings," *Surface & Coatings Technology*, vol. 424, p. 127658, 2021.
- [35] J. Zheng, K. Wen, Y. Liu, L. Gao, Z. Ma, and X. Diao, "Laser irradiation behavior of plasma-sprayed tantalum oxide coatings," *Ceramics International*, vol. 46, pp. 3875-3881, 2020.